Applied Surface Science 731 (2026) 166415

Contents lists available at ScienceDirect

Applied Surface Science

journal homepage: www.elsevier.com/locate/apsusc

Influence of near-edge Laser-Induced Periodic Surface Structures (LIPSS) on the electrical properties of fs-laser-machined ITO microcircuits☆

A. Frechilla [a], E. Martínez [a], J. del Moral [b], C. López-Santos [b,c], J. Frechilla [a], F. Nuñez-Gálvez [b,c], V. López-Flores [b,c], G.F. de la Fuente [a], D. Hülagü [d], J. Bonse [d], A.R. González-Elipe [b], A. Borrás [b], L.A. Angurel [a,*]

[a] Instituto de Nanociencia y Materiales de Aragón, INMA, CSIC-Universidad de Zaragoza, María de Luna 3, 50018 Zaragoza, Spain
[b] Nanotechnology on Surfaces and Plasma, Instituto de Ciencia Materiales de Sevilla, ICMS, CSIC-Universidad de Sevilla, Américo Vespucio 49, 41092 Sevilla, Spain
[c] Dpto. Física Aplicada I. Escuela Politécnica Superior, Universidad de Sevilla, c/ Virgen de África 7, 41011 Sevilla, Spain
[d] Bundesanstalt für Materialforschung und –prüfung (BAM), Unter den Eichen 87, 12205 Berlin, Germany

ARTICLE INFO

Keywords:
ITO
Laser subtractive manufacturing
fs-laser processing
LIPSS
Electrical properties

ABSTRACT

Scalable, cost-effective methods for processing transparent electrodes at the microscale are pivotal to advancing in electrochemistry, optoelectronics, microfluidics, and energy harvesting. In these fields, the precise fabrication of micrometric circuits and patterns plays a critical role in determining device performance, material compatibility, and integration with added-value substrates. In this context, Laser Subtractive Manufacturing stands out as a suitable microfabrication technique for its adaptability to diverse materials and complex configurations, as well as its straightforward scalability, affordability, and eco-friendly nature. However, a challenge in micromachining metals and metal oxides is the inherent formation of Laser-Induced Periodic Surface Structures (LIPSS), which can significantly impair electrical conductivity, particularly when circuit dimensions fall within the micrometer range. Herein, we investigate the micromachining of electrical microcircuits using ultrashort pulse laser systems applied to transparent indium tin oxide (ITO) thin films. We analyze the formation of LIPSS at the edges of the micromachined regions associated with the Gaussian distribution of the energy within the laser spot, and the impact of these structures on the electrical properties of the circuits. Thus, we systematically evaluate the influence of LIPSS orientation and periodicity by fabricating various circuit patterns using femtosecond lasers at green (515 nm) and ultraviolet (UV) (343 nm) wavelengths. A correlation between electrical resistivity measurements and microstructure analysis, as determined by field emission scanning electron and transmission electron microscopy, reveals distinct effects of the formed nanostructures depending on the laser source and its polarization. For the green wavelength, the edge side regions where LIPSS are oriented perpendicular to the ITO track exhibit a resistance higher by a factor just above two compared to those where LIPSS are parallel. Additionally, UV laser processing results in a pronounced reduction of ITO thickness at the boundary between the LIPSS region and the substrate. The mechanisms for the formation of LIPSS with both wavelengths are also discussed. Furthermore, we have determined that in narrow conductive tracks with a width ranging from 6 to 8 μm, the impact of LIPSS is particularly significant because the LIPSS structured region occupies a dominant fraction of the total width.

1. Introduction

Indium Tin Oxide (ITO), typically ≈90% wt% In_2O_3 + 10 wt% SnO_2, is a captivating material due to its low electrical resistivity and high transparency within the visible spectrum. These properties make it one of the most widely used Transparent Conducting Oxides (TCOs) in a variety of advanced applications [1]. ITO is particularly important for the fabrication of transparent electronic circuits [2] and serves as a universal electrode in various devices [3]. For example, ITO is employed in the manufacturing of Liquid-Crystal Displays (LCDs) [3,4], Organic Light Emitting Diodes (OLEDs) [5,6], or solar cells [7,8], and constitutes a promising material for sensing applications [9,10]. These

☆ This article is part of a special issue entitled: 'ICPEPA-2025' published in Applied Surface Science.
* Corresponding author.

https://doi.org/10.1016/j.apsusc.2026.166415
Received 17 November 2025; Received in revised form 30 January 2026; Accepted 20 February 2026
Available online 20 February 2026

technological applications led to the consideration of indium as a critical raw material in the European Union over the past few decades. However, this status has recently changed due to the emergence of new domestic suppliers [11].

The electrical and optical properties of ITO films are highly dependent on their fabrication procedure [12], which directly affects their performance for most applications [5,13]. For many advanced electrical applications, high-resolution patterning of thin films in the form of interconnected lines, paths, or assemblies [7] with characteristic features in the micrometric range constitutes the basis of a large variety of circuit designs. Thus, downsizing the conductive paths for transparent electrodes has paved the way for the development of micro-LEDs [14], high-resolution smart screens [15], biosensors [9], digital microfluidics [16], lab-on-chip platforms [17], and transparent thin-film transistors [18], among others. As a result, various techniques are currently applied to pattern ITO electrode structures with well-defined edges and electrically insulating paths between the conductive tracks. Widely used techniques include photolithography and micro-contact printing procedures. However, these methods are complex, time-consuming, and require multiple processing steps, expensive equipment, and toxic chemicals. These drawbacks emphasize the urgent need for direct non-lithographic patterning strategies for the fabrication of micrometric and well-defined circuit structures using ITO thin films as starting material.

In this context, ultrashort pulse laser micromachining has emerged as a paradigm-shifting technology thanks to its unprecedented precision, control, and versatility. When the laser pulse duration is shorter than the electron–phonon interaction time constant, the deposited optical energy stays confined during the irradiation, reducing accompanying thermal processes in the micromachining. However, after the laser pulse absorption by the electrons of the solid, its lattice is heated up and melting and evaporation/ablation may occur and persist for several nanoseconds or even longer. Consequently, even with these ultrashort laser pulses, there is always a molten volume, but localized in a surface layer, typically with a thickness of up to several tens of nanometers [19]. Nevertheless, compared to longer pulse durations, this so-called “heat-affected zone” (HAZ) is significantly reduced. For this reason and due to the high laser peak intensities involved, ultrashort pulsed lasers have successfully been applied in the processing of all kind of materials [20–24], including ceramics [22], glasses [23] and polymers [24], where thermal components generated during the laser treatment may detrimentally affect the material. The control of the ablation process using these ultrashort pulsed lasers has also been used for the fabrication of electrical circuits from thin films of conductive and non-conductive materials [25,26]. This laser processing technique enables the selective removal of the ITO thin film from certain zones, thereby creating the intended ITO microcircuit patterns [27,28]. This method opens new possibilities for fabricating intricate circuit designs, overcoming traditional limitations associated with conventional manufacturing processes. Furthermore, laser micromachining of ITO thin films offers high flexibility for circuit patterning designs and fast processing times, making it especially attractive for large-scale fabrication. Additionally, laser patterning, as a mask-free technique conducted under ambient conditions, can be easily implemented for repairing applications [12].

Different works have investigated the ablation process associated with the laser micromachining of ITO circuits using a variety of laser sources. Some have reported the application of nanosecond pulsed lasers operating in the ultraviolet (250–350 nm) [2,10] or near-infrared wavelengths (around 1064 nm) [10]. Notably, 355 nm laser radiation has shown promising results for ITO ablation, likely due to the good matching between the photon energy (3.49 eV) and the material bandgap (3.6–3.8 eV) [10] enabling linear energy absorption in the material. Other studies have focused on the use of ultrashort laser pulses with durations in the femtosecond or picosecond range, using lasers with wavelengths between 700 and 800 nm [5,7,8,12,28] or 1030 nm [13]. While thermal effects may degrade patterning precision when using longer pulse durations [10], ultrafast laser ablation has gained increasing relevance due to its enhanced versatility, minimal detrimental thermal effects [29,30] and the possibility to process glass-supported films in superstrate geometry with minimal device damage [9,10,13,31]. In some cases, femtosecond laser patterning has also been complemented with a chemical etching process to complete the removal of the non-irradiated ITO layer [8,28].

One of the effects observed during direct ultrafast laser patterning of ITO thin films is the formation of Laser-Induced Periodic Surface Structures (LIPSS), whose formation is due to the interaction between the laser beam and the material surface [32–35]. These structures can significantly influence the optical and electrical properties of the patterned circuits, leading to anisotropy in surface characteristics that can either enhance or degrade the performance of the final device [35]. LIPSS formation has been widely reported in different materials processed with femtosecond lasers, where a strong dependence has been found on laser wavelength, fluence, number of pulses, and material properties [35–40]. However, their formation in laser micromachined ITO structures, particularly at the edges of conductive tracks of micron-sized electrodes, and their effect in electrical properties remains an open topic asking for further investigation. In order to evaluate its influence on the final performance of the ITO microcircuit, it is important to define the percentage of the width of the conductive track where LIPSS are generated, to evaluate the possible reduction on the electrical conductivity in these regions and to clarify how this can modify the total resistance of the electrical circuit.

In this article, femtosecond Laser Subtractive Manufacturing (LSM) was used to fabricate micro-scale ITO conductive surface patterns. This technique utilizes a laser beam to selectively ablate specific areas of the ITO thin film, creating the “negative” (electrically isolating) space required for the circuit design. The remaining ITO material defines the desired conductive circuit pattern on the substrate. Specifically, we focus on the analysis of the LIPSS formed at the edges of the ITO tracks due to the Gaussian energy distribution of the ultrashort laser pulses. To gain a deeper understanding of the topography, nanostructure characteristics and chemical composition of these transitional zones, we employ multiple characterization techniques, including Field Emission Scanning Electron Microscopy (FESEM), Transmission Electron Microscopy (TEM) and electron probe microanalyzer measurements. Additionally, in order to assess their impact on the electrical behavior of the patterned circuits we propose a model of parallel resistance networks that has been validated with four-probe resistivity measurements at macro and microscales. This study provides new insights into the development of LIPSS in femtosecond laser-processed ITO films and offers valuable guidelines for optimizing the laser patterning process to improve electric microcircuits device performance.

2. Experimental

Fabrication of the electrical circuits was performed by selective laser irradiation on commercial ITO thin films with thicknesses in the range from 100 to 140 (±5) nm, deposited on a 2.5 cm × 2.5 cm sodalime glass substrate (supplied by Xop Glass). The resistivity of the original ITO thin films ρ_{ITO} was measured as $1.6 \cdot 10^{-6}\ \Omega \cdot m$, which is similar to the value reported in the literature for the same range of film thicknesses [1].

2.1. Morphology, chemical, electrical, and optical characterization methods

Surface morphology was analyzed with a FESEM (MERLIN, Carl Zeiss, Oberkochen, Germany) using secondary electron (SE), backscattered electron (BE) and in-lens detectors. The electron beam acceleration voltage was set to 5 kV, enabling a high surface sensitivity. Image post-processing and 2-dimensional fast Fourier transforms (2D-FFT) were applied using the open-source software Gwyddion (vers. 2.61, Czech Metrology Institute, Brno, Czech Republic). To analyze the

topography of cross-section areas near the laser micromachined edges, some lamellas were prepared using a Focused Ion Beam (FIB) in a Dual Beam Helios 650 (FEI company, Hillsboro, OR, USA). Scanning transmission electron microscopy (STEM) imaging of these lamellas was performed in a probe-corrected Titan microscope (Thermo Scientific) operated at 300 kV and equipped with a high brightness X-FEG and a spherical aberration Cs-corrector (CEOS), enabling that the condenser system yields a sub-angstrom probe size. High angle annular dark field (HAADF) images were obtained with a HAADF detector by Fischione (Pittsburgh, PA, USA).

Chemical surface characterization was done with a JXA-iHP200F (JEOL Ltd., Akishima, Japan) electron probe microanalyser, which is based on FESEM and is equipped with a SS-94040SXSER spectrometer. Wavelength-dispersive X-ray spectroscopy (WDS) with high spectral resolution was used to detect possible compositional variations in the ITO thin films near the laser micromachined paths. Specifically, the elements In, Sn, and O were analyzed, using 6 kV electron acceleration voltage and 10 nA beam current for excitation.

The electrical properties were measured with a Keithley 2000 multimeter connected to a 4-point probe station with a distance between voltage contacts of 4.3 mm. All the measurements were performed in air at room temperature. Selected samples were also characterized using a FESEM Zeiss GeminiSEM 300 at 5 kV and electrically characterized with a Kleindiek micromanipulator system in a 4-point probe configuration assisted by a Keithley 2635 multimeter source. For this analysis, the set of tungsten Micro-Pico Probes T4-10 of 3.3 mm length, 10 μm diameter, and ~4 ± 0.1 μm point radius were separated by a distance between voltage contacts of 60 μm (a micrograph of the four probes emplaced on an ITO conductive track is shown in Fig. S1 of Supplementary Information).

The optical properties of the pristine ITO films were characterized by variable angle spectroscopic ellipsometry (SE) using an M2000DI instrument (J.A. Woollam, Lincoln, NE, USA) for three angles of incidence (AOI), i.e., at 65°, 70°, and 75°, respectively. For all AOIs, the ellipsometric transfer data Ψ and Δ were recorded over the spectral range of 250 nm–1000 nm. The sample was probed over an area of 5 × 3 mm^2. Wavelength-dependent values of the optical constants (refractive index n and extinction coefficient k) were derived from least-squares-fits of a two-layer model to the measured ellipsometric entities Ψ and Δ using CompleteEASE Software (J.A. Woollam, Lincoln, NE, USA). While the first (top) layer considered the surface roughness through an effective medium approach (assuming a mixed layer of 50% air and 50% ITO), the second layer consisted of the pure ITO material coated on the underlying soda-lime glass substrate (bulk) forming a smooth interface. The resulting spectral variation of the optical constants is provided in Fig. S2 in the Supplemental Information section. At the two laser wavelengths the optical parameters had the following values: n(343 nm) = 2.2126, k (343 nm) = 0.0118 and n(515 nm) = 1.9252, k(515 nm) = 0.0004.

2.2. Laser machining procedure

A femtosecond laser system (Carbide CB3-40 W + CBM03-2H–3H, Light Conversion, Lithuania) operated at two different wavelengths λ = 515 nm—green or 343 nm—UV (corresponding to the second and third harmonic, respectively) was used to remove the ITO layer in preselected areas. At the working distance, the beam has elliptical Gaussian profiles with $1/e^2$ intensity decay and major axes of ≈ 50 μm (green) and 64 μm (UV), with the main axes ratio of 0.97 and 0.89, respectively. For the experiments, the laser beam was linearly polarized and the pulse duration was 249 fs (green) and 238 fs (UV). All irradiations were performed in air using the same substrate geometry, i.e., with the ITO film side facing the focused laser beam [41].

Several ITO tracks, of widths varying from ≈10 to 1000 μm, were generated using LSM. The original uniform ITO layer was removed in the predefined areas at the two sides of the conductive track using the laser beam scan method that employed a galvanometric mirror system along with a 330 mm focal length f-theta lens, controlled by a dedicated software (Direct Machining Control, UAB, Lithuania). Following the procedure described in [38] and in Fig. S3 the laser processing parameters were selected to achieve homogeneous accumulated laser fluence distribution across the scanned thin film surface. In order to minimize the heat accumulation in the sample material, a repetition frequency of 10 kHz was selected. The laser pulse energies were fixed at 6.55 μJ (λ = 515 nm) and 3.40 μJ (λ = 343 nm). Initially the laser beam processes a line using a scanning speed of 25 mm/s. As a consequence, the distance between the centers of two neighbored laser irradiated spots is 2.5 μm, producing the fluence distribution displayed in Figs. S3(c) and S3(d) in the longitudinal and transverse direction. To process an area, the hatching distance between two consecutive scanning lines was selected as 5 μm. These laser conditions assure that the fluence value at the center of the scanned area is constant and enough to remove completely the ITO layer between the ITO tracks. The laser scan direction was always parallel to the ITO track. For the 515 nm wavelength, four different orientations between the ITO track and the polarization were analysed. For the 343 nm case, however, two configurations were studied with the laser polarization either near-parallel, or near-perpendicular to the track.

3. Results and discussion

Initially, the ITO ablation thresholds for both wavelengths were determined following the method described by Liu [42]. A multipulse analysis was then performed, varying the energy per pulse (E_p) and the number of pulses (N). As an illustrative example of these experiments, Fig. 1 shows the spots produced in a film irradiated with 1 or 10 pulses and E_p = 6.55 μJ (λ = 515 nm) or 3.40 μJ (λ = 343 nm). For a wavelength of 515 nm, the laser-marked region appears nearly circular, with a diameter of approximately 16 μm for N = 1. Conversely, when working with a 343 nm wavelength, the marked region had an elliptical shape, with short and long axis sizes of about 22 μm and 25 μm, respectively. Also, these images demonstrate a higher level of absorption of the UV radiation in comparison with the visible one. At N = 10 and for both wavelengths, a central area was obtained where the ITO layer has been entirely removed (black contrast in the images). A non-steep boundary between the ablated and non-ablated areas characterized this ablation process, where a smooth transition caused by the Gaussian energy distribution of the laser beam could be observed. This transition should be linked with the continuous local variation of pulse fluence from the ablation threshold to zero. In this region between the ablated and the pristine film, the laser modifies the original surface and forms some spatial periodic nanostructures in the form of LIPSS (see zoomed images in the figure). The extension, the topography and chemical and electrical characteristics of these transitional zones should be specifically considered when designing ITO microcircuits. In the following, these zones will be designated as the “edge” of the micromachined areas. Images in Fig. 1 showcase the existence of strong differences in the characteristics of these edge regions depending on the wavelength chosen for ablation.

3.1. Nanostructures at the transition zone between the machined and non-machined regions using λ = 515 nm

Fig. 2 shows SEM images of the edge zone between the ITO track (left) and the glass substrate (right) when machining with λ = 515 nm for different orientations of the nanostructures with respect to the electric track orientation. As observed in the figure, β, the angle between LIPSS orientation and the electric track, takes the following values: β = 75° (Fig. 2(a)), β = −15° (Fig. 2(b)), β = 90° (Fig. 2(c)) and β = 0° (Fig. 2(d)). Four differentiated areas can be identified in these images, highlighted by distinct colour bar segments at the top of the low magnification images: a region where the original ITO has not been modified by the laser treatment (**red**), a laser nanotextured region with a dense LIPSS

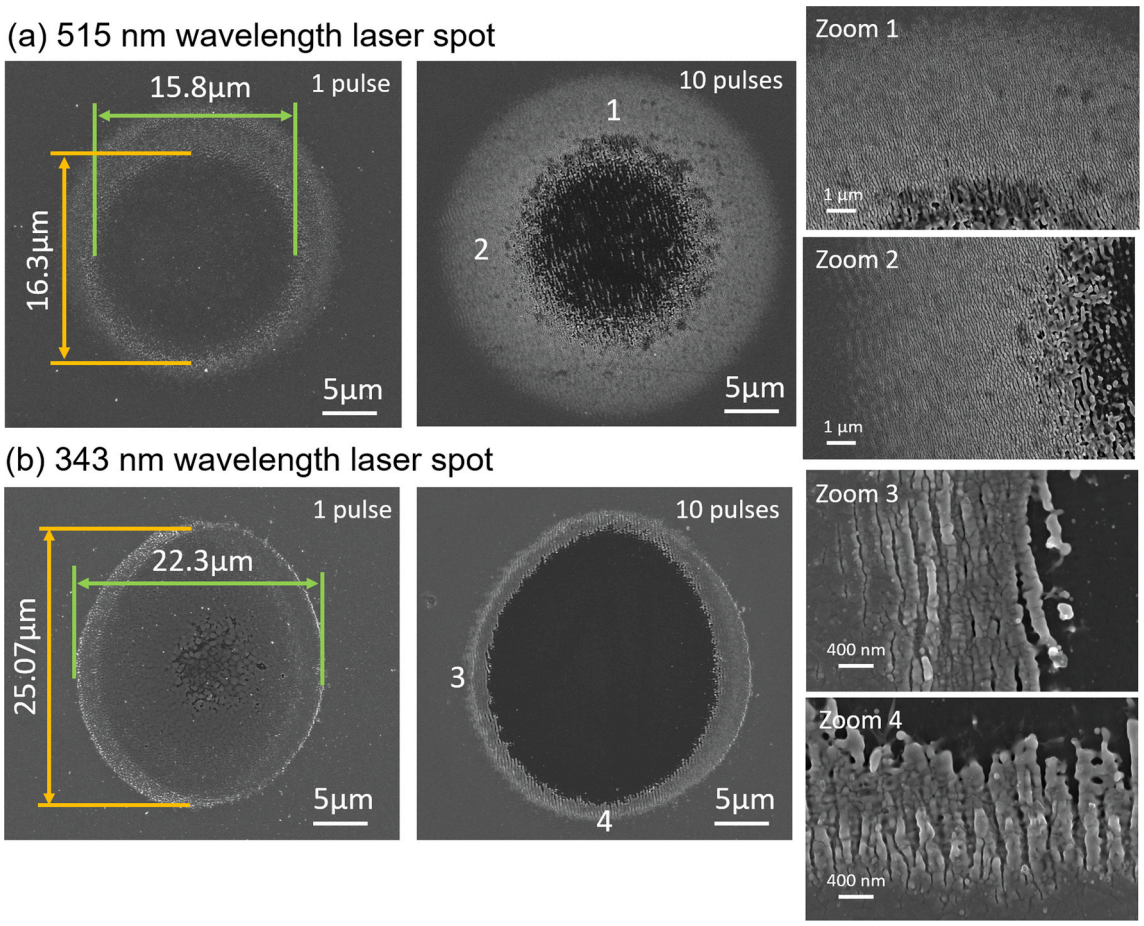

Fig. 1. FESEM micrographs (in lens detector) of the sample surface after having applied 1 or 10 laser pulses in a given position with (a) $\lambda = 515$ nm radiation and $E_p = 6.55$ µJ and (b) $\lambda = 343$ nm and $E_p = 3.40$ µJ. The substrate appears in black contrast in the images.

structure (**green**), a region of isolated LIPSS (**orange**) leading to a loss of film continuity, to finally reach the underlying glass substrate (**blue**), where the ITO layer has been completely removed by the laser treatment. Focusing on the edge zones it is noteworthy that in the four configurations, LIPSS form gradually and become increasingly better-defined as the distance from the pristine zones of the ITO film increases.

The LIPSS ridge orientation is defined here by the direction of the laser beam polarization, which is perpendicular to the direction of the electric field vector of the laser radiation. Towards the border of the non-modified ITO, the spatial periodicities are below 100 nm, far below the laser irradiation wavelength. Thus, these LIPSS can be identified with the typical high spatial frequency LIPSS (HSFL, type I) formed on dielectrics [43] and must emerge here on the ITO film through a collective near-field optical scattering mechanism at surface defects [44].

The evolution of the LIPSS spatial periodicity at the edge of the ITO track was studied by 2D-FFT analysis of several regions, as defined in Fig. 3(a). Thus, from a FESEM image with approximate dimensions $x \times y = 22$ µm $\times$ 15 µm around the ITO track's edge (directions perpendicular $\times$ parallel to the track), several image regions of size $\Delta x \times \Delta y$ ($\Delta x = 1$ µm in most cases and $\Delta y = 15$ µm) were selected, encompassing the 2D-FFT maps of all of them. The corresponding central 1D-profiles perpendicular to the HSFL ridge direction are shown in Fig. 3 (b) for the case of the $\beta = 75°$ configuration. The analysis of these profiles will allow obtaining the spatial periodicity in each position and therefore estimating the spatial periodicity variation in the edge zone, which is displayed in Fig. 3 (c). Fig. S4 of the Supplementary Information shows more details of the performed analysis.

These analyses reveal a clear trend in the evolution of the surface patterns. In locations closer to the pristine ITO film, a high spatial-frequency structure is observed, with periodicities ranging from 90 to 100 nm that are the same for the four values of β. This fine nanostructure likely corresponds to the early-stages of ablation with LIPSS formation, where plasmonic coupling at transient metallic defects and collective interference effects begin to modulate the surface at subwavelength scales, rendering HSFL-I. When approaching the glass substrate region (i.e., upon increasing the coordinate x in the figure), at locations where the local laser fluence is higher due to the Gaussian shape of the laser beam profile, the LIPSS periodicity gradually increases, eventually reaching a regime where two distinct spatial frequencies coexist. Specifically, a dominant well-defined spatial periodicity is observed at $\approx$ 450 – 470 nm, which would correspond to low spatial frequency LIPSS (LSFL, type I), typically expected on absorbing materials at about 0.8 – 0.9 times the laser wavelength [35,39]. Moreover, the mean periodicities of the observed HSFL-I quantified in Fig. 3(c) are in reasonable agreement with the theoretical prediction of $\Lambda_{HSFL} \approx \lambda/(2n)$ [43,44], with n representing the refractive index of ITO. The latter has been determined for our ITO films through ellipsometric measurements as $n = 1.9252$ at $\lambda = 515$ nm (see the Supplementary Information), this resulting in $\Lambda_{HSFL} \approx 133$ nm.

This transition from HSFL-I features over a dual-period region towards a LSFL-I zone has been highlighted in Fig. 3(d). The latter enables observation of how the HSFL-I structures (indicated with red lines in the figure), with periods in the range of 250 $\pm$ 25 nm, are combined to generate a LSFL-I structure (green lines in the figure) with a period close to 473 $\pm$ 15 nm. This behavior suggests a dynamic evolution of the surface interaction mechanism with the laser scanned beam depending on fluence: in the low fluence tail of the Gaussian beam distribution, HSFL-I LIPSS would be seeded and generated at the surface of the ITO

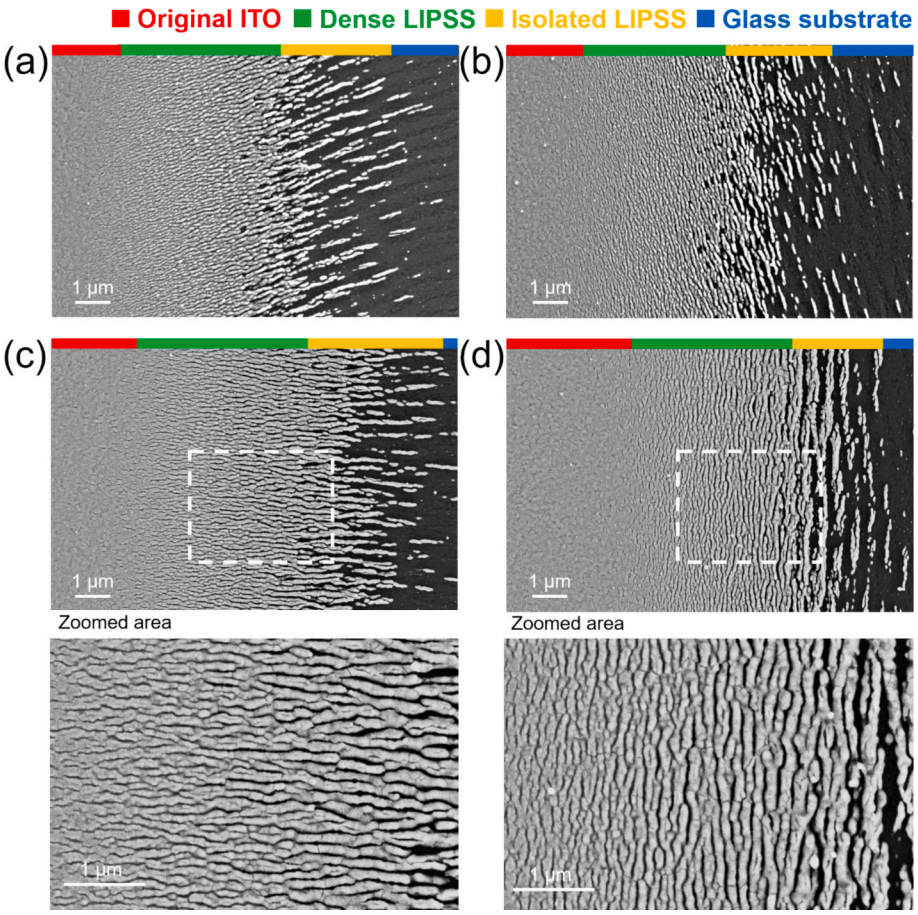

Fig. 2. Top-view FESEM (SE) images of the edges of ITO tracks micromachined with 515 nm fs-laser wavelength for different polarization configurations resulting in different values of β: (a) 75°; (b) −15°; (c) 90° and (d) 0°. The original ITO and the glass substrate appear on the left- and right-hand sides of the micrographs, respectively. The bottom row images display higher magnification micrographs of the areas marked by a dashed white box.

film via the above mentioned collective optical near-field scattering at localized individual plasmonic defects. In the high intensity (center of the Gaussian profile) regions of the scanned laser beam, the combination with multi-pulse incubation effects leads to LSFL-I LIPSS seeding, while formation tales place at the early stage of ablation. This occurs as the result of the well-known Surface Plasmon Polariton (SPP) mediated scattering and interference mechanism [43]. Due to the larger local fluence in this zone, the ITO film is gradually removed upon excitation by several laser pulses, leaving behind the bare glass substrate, where a minimal damage is only identified at the interference maxima of the LSFL-I pattern. Meanwhile, in the transitional (intermediate) fluence range, spatially separated HSFL-I ITO structures can survive at the interference minima of the initially formed LSFL-I LIPSS.

A cross-sectional view of the nanostructured ITO film obtained by TEM is displayed in Fig. 4. The image corresponds to an ITO track edge machined with a 515 nm wavelength laser beam, using a polarization/scanning configuration with $\beta = -15°$. The TEM lamella was taken perpendicular to the LIPSS. The left-hand side of the overview image reported in the top panel corresponds to the pristine ITO film deposited on the glass substrate. Towards the right-hand side direction, some small indents in the film (see area at position 1) of ~20 nm width can be seen. They gradually become more pronounced and deeper (see detailed views at positions 2 and 3), rendering smooth deep trenches with a large depth-to-width aspect ratio ($A \gg 1$). Eventually, some additional shallower and wider near-surface depressions may appear in the ITO film (right-hand side in the top image). It is important to note that despite the surface nanostructuring process, the height of the ITO nanostructures (i.e. LIPSS) remains essentially unchanged throughout the entire textured region covered by this figure, coinciding with the thickness of the original ITO film. The periodic surface structures continue to develop in depth at locations where local fluence of the laser increases. Eventually, they reach the glass substrate, spanning (laterally) a width of several micrometers (≈ 4–6 μm). The observed large aspect ratio A ≫ 1 of the nanostructures in region 3 further confirms that HSFL-I structures are formed in this region [43].

3.2. *Nanostructures in the transition zone between machined and non-machined regions using $\lambda = 343$ nm*

Fig. 5 displays the ITO/glass edge boundaries when machining with a 343 nm laser. Results correspond to both polarization orientations, which lead to LIPSS near-parallel and near-perpendicular to the laser processed track. As expected, LIPSS are also generated in the near-edge transition zone between the unmodified ITO film and the fully laser machined paths. Notable differences are observed with respect to the 515 nm wavelength laser machining. On the one hand, the edge transition region is narrower. On the other, the laser-affected region can be associated mainly with a “dense LIPSS” nanostructure featuring a very sharp transition to the non-affected ITO region. This zone is notably more compact and less extended, suggesting a more abrupt interaction and a localized laser energy deposition when using this wavelength. This transition is also sharper at the end of the machined region, close to the glass substrate, making it more difficult to identify a region with isolated LIPSS.

2D-FFT analysis of the dense LIPSS regions gave a spatial period for the nanostructures of around 300 nm, as expected for LSFL-I.

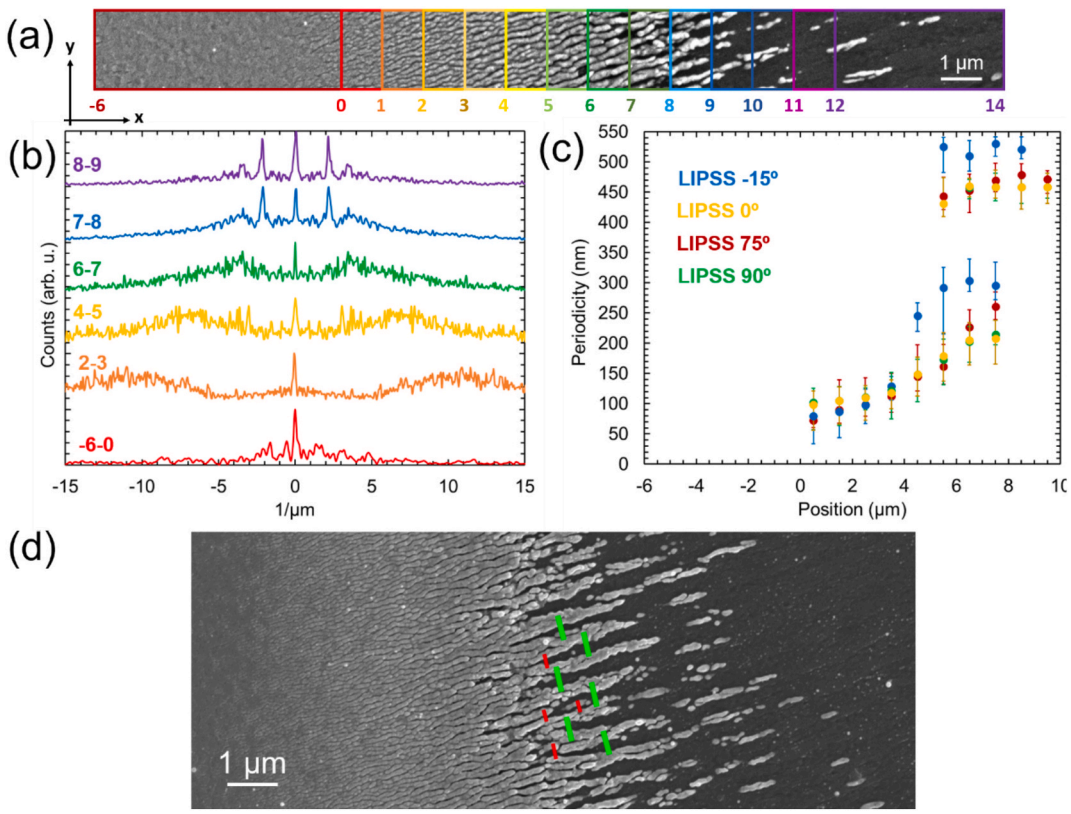

Fig. 3. Analysis of the spatial periodicity evolution along the ITO/glass edge zone for $\lambda = 515$ nm and $\beta = 75°$: Top-view SEM image (a) showing the position ranges of the x-coordinate (in μm) that define the different sections analysed by 2D-FFT. (b) Central 1D-profiles perpendicular to the HSFL ridge direction of the 2D-FFT images, used to quantify the mean spatial periodicity of the LIPSS in different sectors of the edge zone (c). The results obtained for the four analysed configurations (different β values) are also shown in (c) for comparison. (d) FESEM image of the region where HSFL-I LIPSS transit to the LSFL-I. Red and green lines mark, respectively, the spatial distance between centres of adjacent HSFL-I and LSFL-I structures, which are observed in this transitional area. (For interpretation of the references to colour in this figure legend, the reader is referred to the web version of this article.)

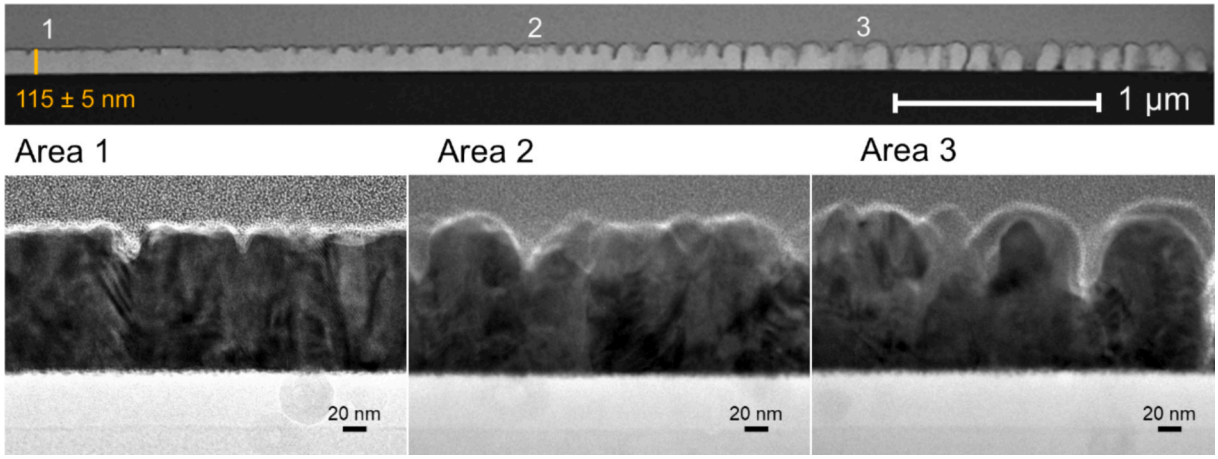

Fig. 4. TEM cross-sectional views of the nanotextured ITO edge zone layer at a lateral position near the unaffected pristine film (left) upon machining with 515 nm laser wavelength (and $\beta = -15°$) (HSFL-I parallel to the ITO track): (Top) Low-magnification HAADF-STEM. The vertical orange line indicates the thickness of the pristine ITO layer. (Bottom) HRTEM images taken at higher magnification at the indicated positions (1 – 3).

Interestingly, HSFL-I were not observed in this case. This is fully consistent with the general observation that HSFL-I structures form predominantly for sub-band gap excitation by ultrashort pulses [43], i.e., when the material is transparent. While the latter condition is strictly fulfilled at $\lambda = 515$ nm (as confirmed by the ellipsometric measurements, see the Supplementary Information S2), the ITO film exhibits a more than one order of magnitude larger absorption coefficient at 343 nm. This allows a relatively linear absorption of the laser radiation, which in combination with the high laser intensities (promoting multi-photon excitation) and with multi-pulse incubation effects, lead to a more efficient promotion of carriers into the conduction band of the ITO [45]. As a consequence, at the selected laser processing conditions, the UV wavelength facilitates the formation of LSFL-I LIPSS via an ultrashort-pulse enabled global transient "SPP-activity", rather than via a

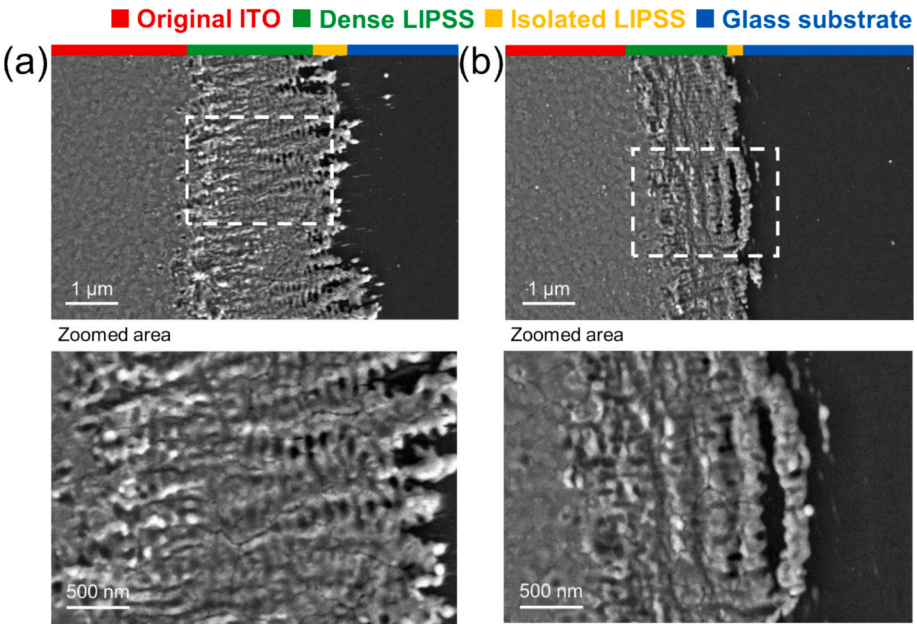

Fig. 5. Top-view FESEM (SE) images of the edges of the ITO track after having applied the laser micromachining treatment with $\lambda = 343$ nm: (a) LIPSS near-perpendicular to the track. (b) LIPSS near-parallel to the track. The original ITO film surface appears on the left-hand side of the micrographs, and the glass substrate (black contrast) on the right-hand one. The top row provides overview images, while the bottom row displays higher magnification images of the areas marked by a dashed white box.

nonlinearly excited defect-mediated local-plasmonic scattering with collective interference as expected for the HSFL-I at 515 nm laser wavelength. Nevertheless, other periodic structures with periods ranging from 50 to 80 nm and oriented perpendicular to these structures were also observed between the LSFL features, in agreement with the observations reported in [46,47].

Fig. 6 displays cross-sectional TEM views of the ITO/glass edge zone developed when machining with the 343 nm laser radiation in the near-parallel configuration. In this case, the laser-affected region exhibits a notable reduction in the ITO thickness, down to nearly 50% of the original value of ~140 nm of the original ITO film. This ablative thinning continues progressively from the thickness of the ITO film to its complete banishment at a distance of approximately 2.7 µm from the beginning of the edge zone. Moreover, the high-aspect-ratio LIPSS trenches are not seen in this specific lamella, in agreement with the SEM observations previously shown in Fig. 5. However, in contrast to the TEM image provided in Fig. 4, the 343 nm laser-induced surface corrugations exhibit a depth-to-width aspect ratio $A < 1$, as expected for LSFL-I structures [43]. The formation of these near-laser-wavelength-sized LSFL-I structures by the UV laser ablation of the ITO films can be accounted for by the laser-induced material removal from the surface (ablation), rather than by a hydrodynamic displacement of the melt with redistribution of material at and above the initial surface plane. In addition, the morphology of the observed small-scale spherical surface heterogeneities is probably the result of the rapid solidification of protuberances formed in the residual melt layer during ablative LIPSS

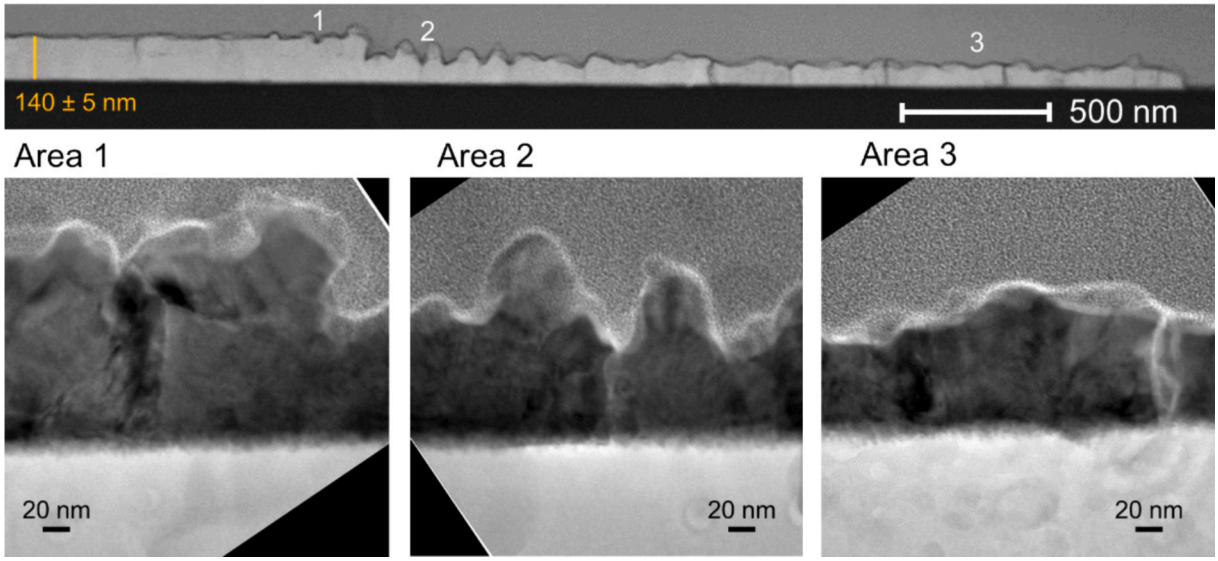

Fig. 6. TEM cross-sectional views of the nanotextured ITO edge zone at the edge of the unaffected pristine film (left) upon machining with 343 nm fs-laser wavelength (LIPSS near-parallel to the ITO path): (Top) Low-magnification HAADF-STEM. The vertical orange line indicates the thickness of the pristine ITO film. (Bottom) HRTEM images taken at higher magnification at the indicated positions.

formation, thus stressing that accompanying transient hydrodynamic effects may be also acting at a few-nanometer-scale [46].

3.3. Chemical analysis of the laser-induced changes in the nanostructured region at the edge of the ITO tracks

WDS maps obtained by electron probe microanalysis provide information about the composition of the laser-affected edge zones. It is important to recall here that this technique has considerably higher spectral resolution and sensitivity compared to energy dispersive X-ray spectroscopy (EDS) [48]. This feature is particularly relevant in this material due to the low Sn/In compositional ratio and the proximity of the X-ray emission lines for Sn and In elements (for example, the $L_{\alpha 1}$ transition of Sn, 3.44 keV, almost overlaps with the $L\beta_1$ transition of In, 3.49 keV).

Fig. 7 displays the results obtained when using either 515 nm ($\beta = -15°$) or 343 nm laser wavelengths in the near-parallel configuration to machine the ITO film. The original ITO and the glass substrate appear, respectively, on the left- and right-hand side panels of this figure. Starting from the non-affected ITO film, a small decrease in the atomic concentration of both elements, Sn and In, is generally observed while approaching to the edge zone. For the 515 nm wavelength, a smooth and moderate decrease or 12% takes place when advancing from $x = 3$ μm to x = 5.5 μm, this latter coinciding with the appearance of high-frequency LIPSS. Then, the decrease is very pronounced (up to a 62%) when approaching the isolated-LIPSS region (marked by an orange colored bar at the top of the graphs). The complete lateral transition zone for the ablation with the 343 nm laser wavelength is considerably narrower and extended from 5.4 μm to 8.0 μm.

In both cases no significant changes in the overall chemical composition of the ITO films are observed, consistently maintaining a constant Sn/In ≈ 0.09 atomic ratio in the edge zone, similar to the composition of the original ITO film. For example, the analysis of the green wavelength ablation experiment shown in Fig. 7(a), in the region between $x = 0$ and 4 μm (original ITO film) the average value of the Sn/In ratio is 0.089 (0.015 std dev), remaining constant at 0.090 (0.012 std dev) at the beginning of the edge zone, 4 μm < x < 6 μm. Then, in the following zone, it exhibits a sharper decrease of both In and Sn amounts (6 μm < x < 9 μm). By contrast, the ratio increases slightly up to 0.096 (0.029 std dev) in the initial 1.7 μm. In general, we can conclude that the observed Sn and In variations are in good correlation with the changes in the film topography at the track's edges observed in TEM images (Figs. 4 and 6). Thus, the decrease of In and Sn elements accompanies an increase of the contribution of the substrate and agrees with that the ITO layer becomes thinner in this zone (or holes start forming). This assessment is further supported by the increase in the oxygen signal, due to the contribution of the glass underneath the ITO, as seen in Figs. S5 and S6. Moreover, the transition onset found for the UV ablation experiment is signaled in Fig. 1(b) by a small but discernible increase of In and Sn (note the higher density of red dots in the map of Fig. 7(b) just at the original/transition area), followed by a sharper decrease of In and Sn. These analyses were performed in other areas obtaining similar results.

3.4. Influence of the laser-generated nanostructures on the electrical properties of ITO tracks

The nanostructured regions formed at the ITO-glass transition zone (i.e., LIPSS zone) are expected to influence the electrical properties of the laser-micromachined tracks. This could be crucial in cases where the width of the transitional zone becomes comparable to the ITO track's width. To quantify these effects for the analysed configurations, several ITO tracks with different widths ranging from 1000 μm down to about 20 μm were micromachined for each case. A picture of a 12-tracks set, each with its corresponding current and voltage contacts for four-point resistance measurements, is shown in Fig. S7 of the supplementary data.

Considering the results of the previous sections, the electrical resistance of the laser-generated ITO fingers has been theoretically modelled as several resistances in parallel. Thus, the central zone of the track, of width w_0, would correspond to the original ITO (red colour in Figs. 2, 5 and 8). Its resistance, R_0, is assumed to retain both, the resistivity (ρ_{ITO}) and thickness (t) of the original ITO film, as this region was not affected by the laser irradiation. Both adjacent edge regions, with a width, w_L,

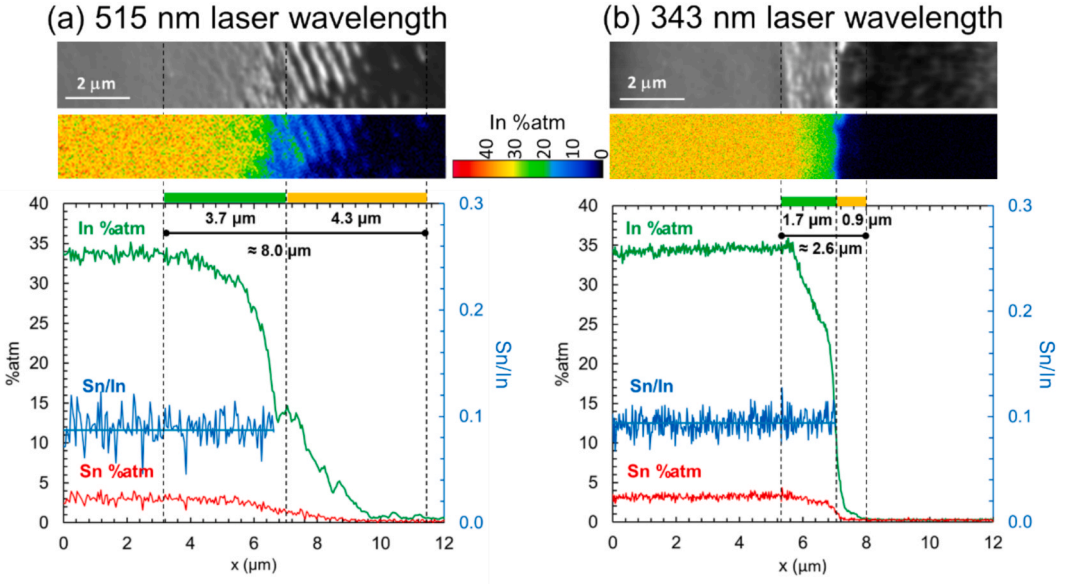

Fig. 7. WDS microanalysis of the ITO films close and at the edge zones using: (a) $\lambda = 515$ nm, $\beta = -15°$ (b) $\lambda = 343$ nm, near-parallel. The original ITO and the glass substrate appear in the left- and righ at-hand sides of the images and graphs, respectively. Top row panels: SEM (SE) images of the analysed areas. Middle row panels: Corresponding WDS maps of In concentration (%atm) in the same areas. Bottom row panels: Line profiles of In, Sn atomic% concentration and Sn/In elemental ratio along both transitions using an averaging line width of 2 μm (i.e., each point in the graph is the average of the values in the map at a given x-position). The darker blue line corresponds to the average Sn/In ratios in this zone, 0.087 (0.015 std dev, green laser wavelength) and 0.094 (0.009 std dev, UV laser wavelength). Note that oxygen concentration was not included here for clarity purposes, but it can be seen in the supplementary file (Figs. S5 and S6). The values of the Sn/In ratio for Sn concentration lower than ≈ 1.5%atm were not included in the figure because of the increment of noise for the selected micro analysis parameters.

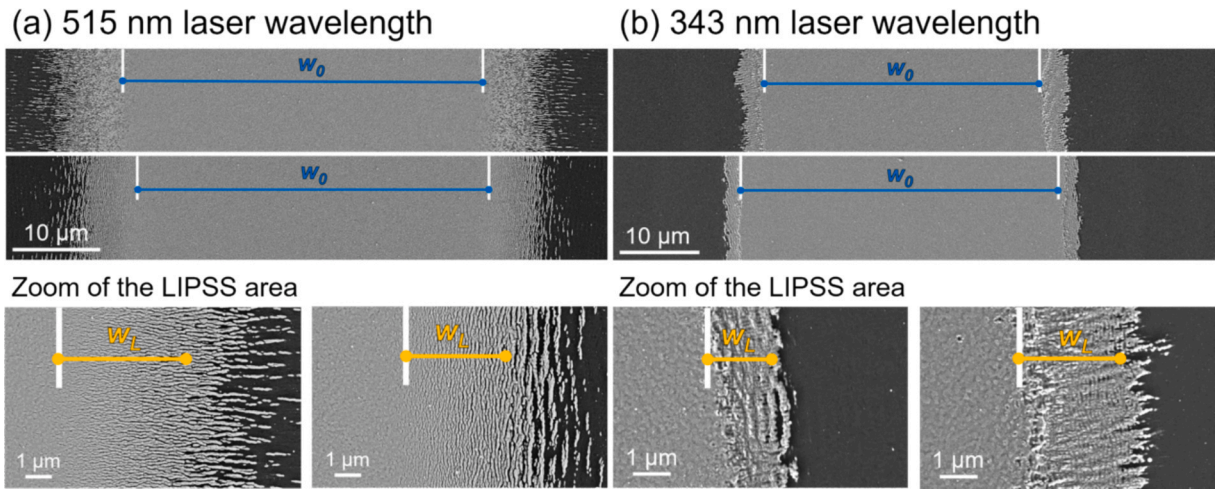

Fig. 8. FESEM (SE) images of four ITO tracks machined with different configurations: (a) 515 nm, $\beta = 0°$ and 90°, (b) 343 nm, LIPSS near-parallel and near-perpendicular. Blue lines correspond to the width of the non-affected areas (w_0). The orange lines in the zoomed images mark the width of the dense-LIPSS areas (w_L), as explained in the text.

green coloured in Figs. 2, 5 and 8, are associated with the presence of dense LIPSS. We assume that both regions on each side would have the same electrical resistance, R_L (for symmetry), which would be different from that of the original ITO film. The electrical behaviour of the system can be modelled with Eqs. (1) and (2).

$$R_0 = \rho_{ITO} \cdot \frac{l}{t \cdot w_0} \tag{1}$$

$$R_L = \rho_L \cdot \frac{l}{t_L \cdot w_L} = \alpha \cdot \left(\frac{\rho_{ITO}}{t}\right) \cdot \frac{l}{w_L} \tag{2}$$

The length between voltage contacts was $l = 4.3$ mm in all cases. The proportionality factor α in Eq. (2) accounts for differences with respect to the original ITO in both, the resistivity (ρ_L) and the effective thickness (t_L) values. This is due to the nano-structural modifications associated to the LIPSS and the resulting reduction of the effective thickness produced by the undulations and material ablation mechanisms involved in their formation [32].

The proposed model considers that the values of R_L and w_L are the same for all the measured tracks fabricated with a given laser wavelength and LIPSS orientation (i.e., α, w_L and R_L are constant for each analysed configuration). In the model, we also assume that the external areas of the edge zones (orange colour in Fig. 8), where LIPSS become spatially and electrically isolated, would not contribute to the total conductivity due to the loss of percolation paths. With the above hypotheses, the estimated track resistance, R, is given by Eq. (3).

$$\frac{1}{R} = \frac{1}{R_0} + \frac{2}{R_L} = \frac{t}{\rho_{ITO} \cdot l} \cdot w_0 + \frac{t}{\rho_{ITO} \cdot l} \cdot \frac{1}{\alpha} \cdot 2w_L = \frac{1}{R_0}\left(1 + \frac{1}{\alpha} \cdot \frac{2w_L}{w_0}\right) \tag{3}$$

Fig. 9 shows the ratio between R_0 and R_{meas}, for varying track widths, $w_{track} = w_0 + 2 \cdot w_L$, in the four analysed configurations. These values follow the expected trend predicted by the proposed model, as shown in Eq. (4).

$$\frac{R_0}{R_{meas}} = 1 + \frac{1}{\alpha} \cdot \frac{2w_L}{w_0} = 1 + \frac{1}{\alpha} \cdot \frac{2w_L}{w_{track} - 2w_L} \tag{4}$$

Table 1 collects the α values estimated for each configuration from this analysis, together with the value of w_L, which was previously determined from FESEM images (this distance was kept fixed for each configuration). When the machining was carried out using the green laser wavelength (Fig. 9(a)), these results indicate that the nano-structured zones near the original ITO contributes significantly to the total resistance of the track, particularly for $w_{track} < 80$–100 μm and LIPSS parallel to the track. Moreover, since the amount of ablated material seems similar for all orientations, the significant difference in the estimated α values (1.5 ($\beta = 0°$) vs 3.7 ($\beta = 90°$)) would reflect an important electrical resistivity anisotropy depending on the LIPSS orientation with respect to the ITO track. Thus, as expected, for the HSFL-I LIPSS featuring isolating deep trenches separating ITO

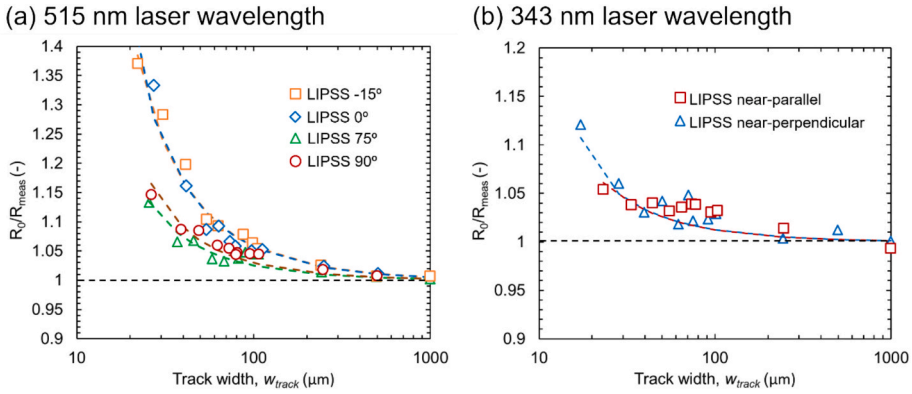

Fig. 9. Measured normalized electrical resistance ratio R_0/R_{meas} of the ITO tracks as a function of the track's width w_{track}, plotted to estimate the contribution of the laser-affected edges to the total resistance of the ITO track for the different configurations: (a) 515 nm, and $\beta = -15°$, 0°, 75° and 90°, (b) 343 nm, LIPSS near-parallel and LIPSS near-perpendicular. The lines represent least-squares-fits to Eq. (4), used to estimate the corresponding values of α, given in Table 1.

Table 1
Values of the parameter α obtained from the proposed resistivity model and average width of the edge, w_L, as estimated from FESEM images.

Laser wavelength and LIPSS orientation with the ITO tracks	w_L (μm)	α
515 nm, −15°	4.1 ± 0.4 μm	1.5 ± 0.1
515 nm, 0°	4.0 ± 0.5 μm	1.5 ± 0.2
515 nm, 75°	4.1 ± 0.4 μm	3.5 ± 0.5
515 nm, 90°	5.0 ± 0.5 μm	3.7 ± 0.4
343 nm, near-perpendicular	2.0 ± 0.3 μm	2.5 ± 0.5
343 nm, near-parallel	1.8 ± 0.3 μm	2.5 ± 0.5

nanostructures ($A \gg 1$), the resistivity of the laser nanotextured region is higher when LIPSS are aligned perpendicular to the ITO track, the value being higher by a factor just above two as compared with the configuration of parallel LIPSS.

On the other hand, when machining was done using UV laser wavelength (Fig. 9(b)) it was not possible to estimate with accuracy any anisotropy, probably because of the effect of the high amount of ablated material in this case, as discussed in previous Sections 3.1 and 3.2. Moreover, the surface corrugations of the resulting LSFL-I nanostructures exhibited a relatively shallow modulation ($A < 1$) and good lateral interconnection, i.e., a percolated morphology promoting an effective current passage across adjacent structures and mitigating orientation-dependent effects. From these considerations, it can be concluded that with this wavelength it is possible to neglect the contribution of the laser-affected edge regions to the total resistance R, within 5% accuracy, even for the narrowest conductive ITO tracks ($w_{track} > \approx$ 20–25 μm), as observed in the figure.

One of the main objectives of this study was to evaluate the influence of the generated LIPSS on the electrical conductivity of laser-processed ITO microcircuits. According to these results, this goal can be best achieved employing UV laser radiation with LIPSS (type LSFL-I) oriented parallel to the electrical track, i.e., by selecting a laser beam polarization perpendicular to it. Under these conditions the laser spatial affected region is minimised (1.8 ± 0.3 μm), thereby preserving the conductive properties of the original film to a greater extent and fully removing the ITO from the intended non-conductive area. On the other hand, the measured resistivity can be easily estimated with rather good accuracy (typically within 2–3%) using the proposed simple parallel circuit resistance model. Conversely, the use of green laser wavelengths to fabricate ITO paths of size w_{track} >20–30 μm can neither be discarded because the lowest α parameter value (≈1.5) was obtained using the green wavelength with LIPSS (type LSFL-I and HSFL-I) oriented parallel to the electrical path.

It is important to distinguish between the pitch, i.e., nominal distance between the laser paths, and the effective width of the machined circuit defined by the laser-affected zone. This difference is more pronounced for the green wavelength because these conditions give rise to larger w_L values, which will significantly influence the final electrical performance of the circuit track. In any case, the influence of the generated surface nanostructures on ITO becomes prominent for track widths narrower than 80 μm, as observed in Fig. 9. In this context, a proper analysis based on the proposed or a similar resistance model would be crucial for assessing the real electrical behaviour of the produced electrical circuits using a Laser Subtractive Manufacturing approach.

In order to explore the limits of our experimental approach, a series of conductive ITO tracks with widths from around 70–80 μm down to a few micrometres were machined for each configuration, while their resistance was measured "in-situ" in a SEM with a 4-point probe micromanipulator setup. Note that different sample pieces of ITO thin films with similar thickness (≈ 115–140 nm) were used for these tests. Fig. 10 shows two representative FESEM images of these narrow tracks machined with green ($\beta = 75°$) or UV (near-perpendicular configuration) wavelength lasers in order to highlight the differences. Despite the similar widths along the length of the two lines, about 8–9 μm, the tracks exhibit very different topographies. Thus, the one obtained at a laser wavelength of 515 nm is completely nanostructured and made of well-defined LIPSS extended up to the centre of the track. Conversely, the track micromachined with the 343 nm wavelength laser preserved a homogeneous central band of the original ITO film, with ≈3.5 ± 0.5 μm in width. The plot of the measured electrical resistance as a function of the overall ITO track width (Fig. 10(c)) reflects the effect of this continuous band as a large decrease in the track resistance for widths at around 10 μm. The influence of the orientation of the LIPSS with respect to the current direction is also noticeable when comparing the different LIPSS orientations.

3.5. Fabrication of electrical circuits

Based on the obtained results, several laser-machined circuits were fabricated as proofs of concept of the developed laser-based technology. Whether the objective is to optimize signal integrity in high-frequency applications or to maintain uniform resistance across conductive tracks, the ability to fine-tune and regulate the widths of both machined regions and the remaining ITO lines in a contactless manner is paramount for achieving the desired circuit performance and reliability. The chosen circuit designs incorporated multiple sets of parallel ITO tracks, which were machined with different widths and distances between them. An example of these test samples is presented in Fig. 11.

Two circuits were machined with the UV radiation using the scheme presented in the centre of the top image for the two configurations, either with LIPSS oriented near-parallel or near-perpendicular to the electrical track direction. Circuits consist of 12 ITO tracks with a length of 4 mm and a thickness of 100 nm in a configuration enabling that the total resistance of the circuit can be measured using a four-point probe. The ITO was removed between two conductive tracks by micromachining with a single laser scanned line at 25 mm/s, a frequency of 10 kHz and an energy of 12.8 μJ/pulse. The distance between two scanned lines was 70 μm. Considering the elliptical shape of the laser spot, the width of the machined lines depends on the scanning orientation. The exact values for w_0 are collected on Table 2. It is also noteworthy that in both configurations it is also observed that the first and the last tracks of the set were slightly wider than the rest (c.f. top panels in Fig. 11). Meanwhile, the bottom left part of the figure shows some details of the connections between two consecutive tracks for the case of the near-perpendicular configuration and the LIPSS generated in both configurations. As indicated in Table 2, the width of the region covered by LIPSS is 1.8 μm and 2 μm in the near-parallel and near-perpendicular configurations, respectively. Adding the resistances associated to each path, the estimated values of R_0 presented on Table 2 were obtained. The influence of LIPSS within each track was estimated using Eq. (4) and the α values presented in Table 1, giving the expected values of R, 22.0 kΩ and 30.9 kΩ for the near-parallel and the near-perpendicular configurations, respectively. These estimations indicate that, in the first case, the correction associated to the generated LIPSS is 4.3%, while in the second one, it is 6.9%. The experimental values measured in the two circuits were 21.2 kΩ and 30.9 kΩ, very close to the estimated R values.

The high quality of the obtained circuit supports that this laser technology has a great potential within the industrial realm. It has been demonstrated that, in addition to precise control over all variables of laser micromachining, scalability can be achieved, leveraging industrial manufacturing processes such as batch production or processing of large surfaces. This represents a starting point for implementing thin film micromachining of transparent conductive oxide thin films or even conducting polymers on an industrial scale, providing a competitive

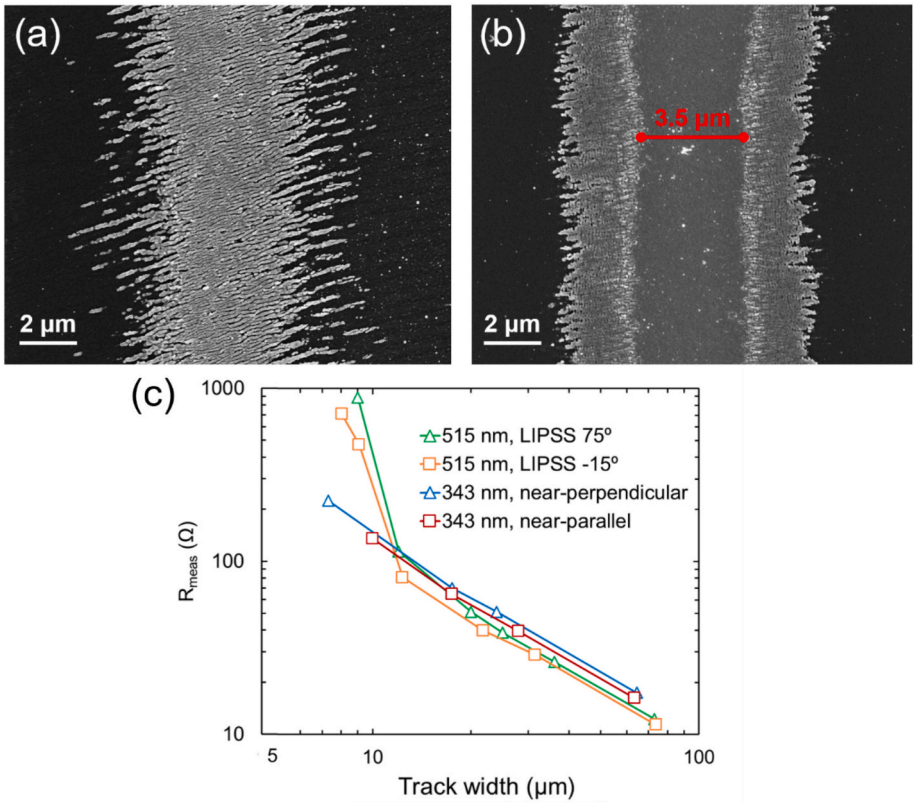

Fig. 10. Top-view FESEM (inlens) images of narrow ITO tracks (bright regions) micromachined with (a) $\lambda = 515$ nm, $\beta = 75°$, and (b) $\lambda = 343$ nm, near-perpendicular. The segment in (b) marks the average width (3.5 μm) of the pristine ITO area. (c) Measured resistance for tracks of different widths for different configurations, using a distance between voltage contacts of ≈ 60 μm.

advantage over more traditional techniques.

4. Conclusions

This study provides a comprehensive analysis of the impact of laser-induced periodic surface structures (LIPSS) on the electrical properties of laser micromachined 100-140 nm thick ITO films. The work thereby highlights the distinct effects of laser wavelength on LIPSS morphology. UV (343 nm) and green (515 nm) wavelengths produce markedly different structures, owing to variations on energy deposition with the ITO film and the occurrence of intra-pulse scattering/interference effects. UV laser radiation yields sharper lateral transitions between the pristine and machined regions, reducing the zones of accompanying LIPSS, whereas green laser radiation results in smoother transitions and wider nanotextured regions. These differences have been explained through the formation of different type of submicrometric LIPSS (HSFL-I and LSFL-I) ruled by the wavelength of the ultrashort laser pulses. Moreover, no significant changes in the overall chemical composition of the ITO films were observed between pristine and the laser nanostructured (percolative) regions at the edges, maintaining a constant Sn/In ≈0.09 atomic ratio.

Through the measurement of the electrical resistance in different series of ITO tracks of variable width it has been demonstrated that LIPSS orientation and periodicity play an important role in the circuit electrical properties. In the case of the UV laser, two series were machined with polarization near-parallel or near-perpendicular to the ITO tracks. In the case of the green laser wavelength, four orientations of LIPSS were analyzed; $\beta = -15°$, 0°, 75° and 90°. For that laser wavelength, the orientation of the LIPSS markedly influences the electrical behavior: circuits with LIPSS oriented at angles $\beta = 75°$ and 90° to the electrical tracks exhibit greater resistivity than those with $\beta = -15°$ and 0° orientations. Using a simple electrical resistance model, it is estimated that the contribution of LIPSS-zones become significant as ITO track's widths decrease below ≈80 μm, up to about 15% or 40% for ≈25 μm-wide tracks with LIPSS oriented perpendicular or parallel to the track, respectively. In contrast, when machining with the UV wavelength, such anisotropy could not be accurately quantified. In the latter, even for narrow conductive ITO lines (≈ 25–30 μm), the contribution of the laser-affected edge regions to the total resistance can be neglected within an accuracy of about 5%. These results stress the importance of tailoring LIPSS characteristics to optimize electrical conductivity in laser micromachined circuits.

Overall, these findings establish laser micromachining as a precise and scalable method for the laser-fabrication of thin-film based microelectronic circuits. The ability to control LIPSS morphology and distribution offers significant potential for tailoring electrical properties to meet specific application requirements. Future work should focus on integrating these optimized circuits into functional devices, exploring their application in fields such as sensors, displays, and photovoltaics. Additionally, advancements in laser technology and parameter optimization could further enhance the precision and efficiency of this micromachining approach.

CRediT authorship contribution statement

A. Frechilla: Investigation. **E. Martínez:** Writing – review & editing, Methodology, Investigation, Formal analysis, Conceptualization. **J. del Moral:** Investigation, Formal analysis. **C. López-Santos:** Writing – review & editing, Investigation. **J. Frechilla:** Investigation. **F. Nuñez-Gálvez:** Investigation. **V. López-Flores:** Investigation. **G.F. de la Fuente:** Writing – review & editing, Conceptualization. **D. Hülagü:** Investigation, Formal analysis. **J. Bonse:** Writing – review & editing, Validation, Investigation, Conceptualization. **A.R. González-Elipe:** Writing – review & editing, Methodology, Formal analysis,

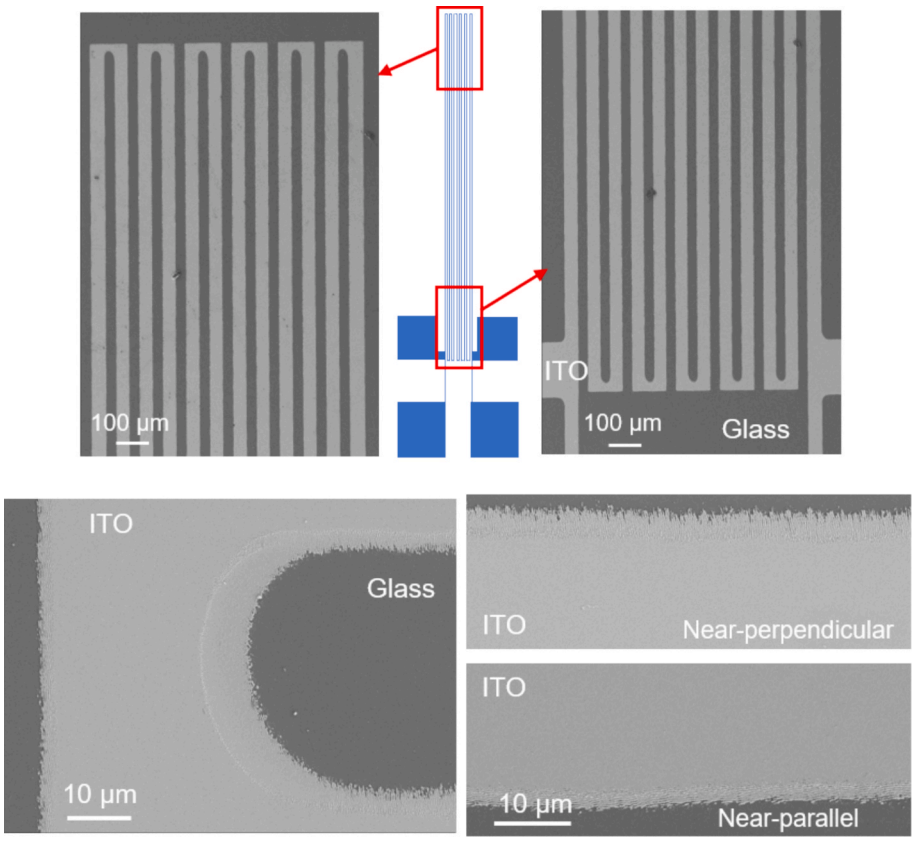

Fig. 11. Top: Scheme and FESEM images of the two ends of the 12 paths of the micromachined circuits using the 343 nm radiation. Bottom: (Left) Detail of the end of one of the paths in the circuit micromachined with the near-perpendicular configuration. (Right) Details of the regions with LIPSS in the two configurations. ITO is characterized by a grey contrast in the images and the glass with a black one.

Table 2
Geometrical factors of the machined microcircuits in both configurations and estimated R_0 and R values deduced using Eqs. (1) and (3). Measured resistance of the circuits, R_{meas}.

Circuit	w_0 (µm) Tracks 1–12	w_0 (µm) Tracks 2–11	w_L (µm)	R_0 (kΩ)	R (kΩ)	R_0/R	R_{meas} (kΩ))
Near-parallel	38.5	33.2	1.8	23.0	22.0	1.043	21.2
Near-perpendicular	27.3	22.6	2	33.0	30.9	1.069	30.9

Conceptualization. **A. Borrás:** Writing – review & editing, Methodology, Funding acquisition, Conceptualization. **L.A. Angurel:** Writing – review & editing, Supervision, Project administration, Methodology, Conceptualization.

Declaration of competing interest

The authors declare that they have no known competing financial interests or personal relationships that could have appeared to influence the work reported in this paper.

Acknowledgments

The authors are grateful for funding from the European Commission EU H2020 program under grant agreement 899352 (FETOPEN-01-2018-2019-2020 – SOUNDofICE), from the Spanish research projects PID2020-113034RB-I00 (funded by MCIN/AEI/ 10.13039/501100011033), PID2023-146041OB-C21 (funded by MICIU/AEI/ 10.13039/501100011033 and ERDF/EU) and TED2021-130916B-I00 (funded by MICIU/AEI/10.13039/501100011033, ERDF (FEDER) A way of making Europe, Fondos Nextgeneration EU and Plan de Recuperación, Transformación y Resiliencia) and from the Government of Aragón (Research Group T54_23R). Authors also thank the use of Servicio General de Apoyo a la Investigación – SAI and the Spanish National Facility ELECMI ICTS, node "Laboratorio de Microscopías Avanzadas (LMA)" at Universidad de Zaragoza and Servicio de Microscopía Electrónica de Barrido de Alta Resolución at Universidad Pablo de Olavide.

Appendix A. Supplementary data

Supplementary data to this article can be found online at https://doi.org/10.1016/j.apsusc.2026.166415.

Data availability

Data are available at: https://doi.org/10.5281/zenodo.17206942

References

[1] M.J. Alam, D.C. Cameron, Optical and electrical properties of transparent conductive ITO thin films deposited by sol-gel process, Thin Solid Films 377–378 (2000) 455–459, https://doi.org/10.1016/S0040-6090(00)01369-9.
[2] G. Singh, H. Sheokand, S. Ghosh, K.V. Srivastava, J. Ramkumar, S.A. Ramakrishna, Excimer laser micromachining of indium tin oxide for fabrication of optically

transparent metamaterial absorbers, Appl. Phys. A 125 (2019) 23, https://doi.org/10.1007/s00339-018-2013-7.
[3] T.R. Chou, S.H. Chen, Y.T. Chiang, Y.T. Lin, C.Y. Chao, Highly conductive PEDOT: PSS films by post-treatment with dimethyl sulfoxide for ITO-free liquid crystal display, J. Mater. Chem. C 3 (2015) 3760–3766, https://doi.org/10.1039/C5TC00276A.
[4] T. Minami, Present status of transparent conducting oxide thin-film development for Indium-Tin-Oxide (ITO) substitutes, Thin Solid Films 516 (2008) 5822–5828, https://doi.org/10.1016/j.tsf.2007.10.063.
[5] M. Park, B.H. Chon, H.S. Kim, S.C. Jeoung, D. Kim, J.I. Lee, H.Y. Chu, H.R. Kim, Ultrafast laser ablation of indium tin oxide thin films for organic light-emitting diode application, Opt. Lasers Eng. 44 (2006) 138–146, https://doi.org/10.1016/j.optlaseeng.2005.03.009.
[6] J.S. Kim, R.H. Friend, F. Cacialli, Improved operational stability of polyfluorene-based organic light-emitting diodes with plasma-treated indium–tin–oxide anodes, Appl. Phys. Lett. 74 (1999) 3084–3086, https://doi.org/10.1063/1.124069.
[7] Q. Bian, X. Yu, B. Zhao, Z. Chang, S. Lei, Femtosecond laser ablation of indium tin-oxide narrow grooves for thin film solar cells, Opt. Laser Technol. 45 (2013) 395–401, doi: j.optlastec.2012.06.018.
[8] C.W. Cheng, W.C. Shen, C.Y. Lin, Y.J. Lee, J.S. Chen, Fabrication of micro/nano crystalline ITO structures by femtosecond laser pulses, Appl. Phys. A 101 (2010) 243–248, https://doi.org/10.1007/s00339-010-5810-1.
[9] E.B. Aydın, M.K. Sezgintürk, Indium tin oxide (ITO): a promising material in biosensing technology, TrAC - Trends Anal. Chem. 97 (2017) 309–315, https://doi.org/10.1016/j.trac.2017.09.021.
[10] C. Molpeceres, S. Lauzurica, J.L. Ocaña, J.J. Gandía, L. Urbina, J. Cárabe, Microprocessing of ITO and a-Si thin films using ns laser sources, J. Micromech. Microeng. 15 (2005) 1271–1278, https://doi.org/10.1088/0960-1317/15/6/019.
[11] European Commission. Critical and strategic materials [Internet]. RMIS – Raw Materials Information System. 2023. Available from: https://rmis.jrc.ec.europa.eu/eu-critical-raw-materials.
[12] H.W. Choi, D.F. Farson, J. Bovatsek, A. Arai, D. Ashkenasi, Direct-write patterning of indium-tin-oxide film by high pulse repetition frequency femtosecond laser ablation, Appl. Opt. 46 (2007) 5792–5799, https://doi.org/10.1364/ao.46.005792.
[13] S. Krause, P.T. Miclea, F. Steudel, S. Schweizer, G. Seifert, Precise microstructuring of indium-tin oxide thin films on glass by selective femtosecond laser ablation, EPJ Photovolt. 4 (2013) 40601, https://doi.org/10.1051/epjpv/2012013.
[14] C. Altinkaya, M.A. Najmi, D. Lida, K. Ohkawa, Light extraction improvement via ITO p-electrodes for InGaN red micro-LEDs emitting at 640 nm, Opt. Contin. 4 (2025) 1040–1050, https://doi.org/10.1364/OPTCON.559350.
[15] R.S. Datta, N. Syed, A. Zavabeti, A. Jannat, M. Mohiuddin, M. Rokunuzzaman, B. Y. Zhang, M.A. Rahman, P. Atkin, K.A. Messalea, M.B. Ghasemian, E.D. Gaspera, S. Bhattacharyya, M.S. Fuhrer, S.P. Russo, C.F. McConville, D. Esrafilzadeh, K. Kalantar-Zadeh, T. Daeneke, Flexible two dimensional indium tin oxide fabricated using a liquid metal printing technique, Nat. Electon. 3 (2020) 51–58, https://doi.org/10.1038/s41928-019-0353-8.
[16] J. Nsabimana, Y. Wang, Q. Ruan, T. Li, H. Shen, C. Yang, Z. Zhu, An electrochemical method for a rapid and sensitive immunoassay on digital microfluidics with integrated indium tin oxide electrodes coated on a PET film, Analyst 146 (2021) 4473–4479, https://doi.org/10.1039/d1an00513h.
[17] D.T. Papanastasiou, A. Sekkat, V.H. Nguyen, C. Jiménez, D. Muñoz-Rojas, F. Bruckert, D. Bellet, Stable flecible transparent electrodes for localized heating of lab-on-a-chip devices, Adv. Mater. Technol. 8 (2023) 2200563, https://doi.org/10.1002/admt.202200563.
[18] J.H. Park, H.J. Seok, S.H. Jung, H.K. Cho, H.K. Kim, Rapid thermal annealing effect of transparent ITO source and drain electrode for transparent thin film transistors, Ceram. Int. 47 (2021) 3149–3158, https://doi.org/10.1016/j.ceramint.2020.09.152.
[19] L. Rihakova, H. Chmelickovaa, Laser micromachining of glass, silicon and ceramics, Adv. Mat. Sci. Eng. 2015 (2015) 584952, https://doi.org/10.1155/2015/584952.
[20] K.M. Tanvir Ahmmed, C. Grambow, A.M. Kietzig, Fabrication of micro/nano structures on metals by femtosecond laser micromachining, Micromachines 5 (2014) 1219–1253, https://doi.org/10.3390/mi5041219.
[21] K. Jiang, P. Zhang, A. Song, T. Sun, Y. Chen, H. Shi, H. Yan, Q. Lu, G. Chen, A review of ultra-short pulse laser micromachining of wide bandgap semiconductor materials: SiC and GaN, Mat. Sci. Semicond. Proc. 180 (2024) 108559, https://doi.org/10.1016/j.mssp.2024.108559.
[22] J. Han, B. Göksel, S. Mohajernia, M.S. Killian, J. Vleugels, A. Braem, S. Castagne, Ultrashort pulsed laser ablation of zirconia thoughened alumina: material removal mechanism and surface characteristics, Appl. Surf. Sci. 615 (2023) 156407, https://doi.org/10.1016/j.apsusc.2023.156407.
[23] Y. Yang, K. Bischoff, D. Mücke, C. Esen, R. Hellmann, UV-ultrashort pulsed laser ablation of fused silica, Jour. Laser Appl. 36 (2024) 012019, https://doi.org/10.2351/7.0001197.
[24] J. Molinuevo, E. Rodríguez-Vidal, I. Quintana, M. Morales, C. Molpeceres, Experimental investigation into ultrafast laser ablation of polypropylene by burst and single pulse modes, Optics Laser Technol. 152 (2022) 108098, https://doi.org/10.1016/j.optlastec.2022.108098.
[25] Z. Wang, Z. Huang, N. Lu, J. Guan, Y. Hu, Energy transfer and patterning characteristics in pulsed-laser subtractive manufacturing of single layer of MoS_2, Int. J. Heat Mass Transf. 204 (2023) 123873, https://doi.org/10.1016/j.ijheatmasstransfer.2023.123873.
[26] C. Zheng, Y. Cai, P. Zhang, T. Zhang, J. Aslam, Q. Song, Z. Liu, Femtosecond laser precision machining of carbon film based on aramid paper substrate, J. Manuf. Process. 119 (2024) 57–65, https://doi.org/10.1016/j.jmapro.2024.03.061.
[27] S.F. Tseng, W.T. Hsiao, K.C. Huang, D. Chiang, M.F. Chen, C.P. Chou, Laser scribing of indium tin oxide (ITO) thin films deposited on various substrates for touch panels, Appl. Surf. Sci. 257 (2010) 1487–1494, https://doi.org/10.1016/j.apsusc.2010.08.080.
[28] C.W. Cheng, C.Y. Lin, High precision patterning of ITO using femtosecond laser annealing process, Appl. Surf. Sci. 314 (2014) 215–220, https://doi.org/10.1016/j.apsusc.2014.06.174.
[29] J. Bonse, J.M. Wrobel, K.W. Brzezinka, N. Esser, W. Kautek, Femtosecond laser irradiation of indium phosphide in air: Raman spectroscopic and atomic force microscopic investigations, Appl. Surf. Sci. 202 (2002) 272–282, https://doi.org/10.1016/S0169-4332(02)00948-0.
[30] M. Lenzner, J. Krüger, W. Kautek, F. Krausz, Precision laser ablation of dielectrics in the 10 fs regime, Appl. Phys. A 68 (1999) 369–371, https://doi.org/10.1007/s003390050906.
[31] J. Bovatsek, A. Tamhankar, R.S. Patel, N.M. Bulgakova, J. Bonse, Thin film removal mechanisms in ns-laser processing of photovoltaic materials, Thin Solid Films 518 (2010) 2897–2904, https://doi.org/10.1016/j.tsf.2009.10.135.
[32] L. Porta-Velilla, E. Martínez, A. Frechilla, M. Castro, G.F. de la Fuente, J. Bonse, L. A. Angurel, Grain orientation, angle of incidence, and beam polarization effects on ultraviolet 300 ps-laser-induced nanostructures on 316L stainless steel, Laser Photonics Rev. 18 (2024) 2300589, https://doi.org/10.1002/lpor.202300589.
[33] Q. Jiang, Y. Zhang, Y. Xu, S. Zhang, D. Feng, T. Jia, Z. Sun, J. Qiu, Extremely high-quality periodic structures on ITO film efficiently fabricated by femtosecond pulse train output from a frequency-doubled Fabry – Perot cavity, Nanomaterials 13 (2023) 1510, https://doi.org/10.3390/nano13091510.
[34] J. Bonse, S.V. Kirner, J. Krüger, Laser-Induced Periodic Surface Structures (LIPSS), in: K. Sugioka (Ed.), Handbook of Laser Micro-and Nano-Engineering, Springer, Cham, 2021, p. 879, https://doi.org/10.1007/978-3-030-63647-0_17.
[35] J. Bonse, Quo vadis LIPSS?—recent and future trends on laser-induced periodic surface structures, Nanomaterials 10 (2020) 1950, https://doi.org/10.3390/nano10101950.
[36] C. López-Santos, D. Puerto, J. Siegel, M. Macías-Montero, C. Florian, J. Gil-Rostra, V. López-Flores, A. Borrás, A.R. González-Elipe, J. Solís, Anisotropic resistivity surfaces produced in ITO Films by laser-induced nanoscale self-organization, Adv. Opt. Mater. 9 (2021) 2001086, https://doi.org/10.1002/adom.202001086.
[37] R. Wonneberger, S. Gräf, J. Bonse, W. Wisniewski, K. Freiberg, M. Hafermann, C. Ronning, F.A. Müller, A. Undisz, Tracing the formation of femtosecond laser-induced periodic surface structures (LIPSS) by implanted markers, ACS Appl. Mater. Interfaces 17 (2025) 2462–2468, https://doi.org/10.1021/acsami.4c14777.
[38] L. Porta-Velilla, N. Turan, Á. Cubero, W. Shao, H. Li, G.F. De la Fuente, E. Martínez, A. Larrea, M. Castro, H. Koralay, S. Cavdar, J. Bonse, L.A. Angurel, Highly regular hexagonally-arranged nanostructures on Ni-W alloy tapes upon irradiation with ultrashort UV laser pulses, Nanomaterials 14 (2022) 2380, https://doi.org/10.3390/nano12142380.
[39] J. Bonse, J. Krüger, S. Höhm, A. Rosenfeld, Femtosecond laser-induced periodic surface structures, J. Laser Appl. 24 (2012) 042006, https://doi.org/10.2351/1.4712658.
[40] A. Frechilla, A. Sekkat, M. Dibenedetto, F. lo Presti, L. Porta-Velilla, E. Martínez, G. F. De la Fuente, L.A. Angurel, D. Muñoz-Rojas, Generating colours through a novel approach based on spatial ALD and laser processing, Mater. Today Adv. 19 (2023) 100414, https://doi.org/10.1016/j.mtadv.2023.100414.
[41] J. Bonse, J. Krüger, Structuring of thin films by ultrashort laser pulses, Appl. Phys. A 129 (2023) 14, https://doi.org/10.1007/s00339-022-06229-x.
[42] J.M. Liu, Simple technique for measurements of pulsed Gaussian-beam spot sizes, Opt. Lett. 7 (1982) 196–198, https://doi.org/10.1364/OL.7.000196.
[43] J. Bonse, S. Gräf, Maxwell meets marangoni—a review of theories on laser-induced periodic surface structures, Laser Photonics Rev. 14 (2020) 2000215, https://doi.org/10.1002/lpor.202000215.
[44] A. Rudenko, J.-P. Colombier, S. Höhm, A. Rosenfeld, J. Krüger, J. Bonse, T.E. Itina, Spontaneous periodic ordering on the surface and in the bulk of dielectrics irradiated by ultrafast laser: a shared electromagnetic origin, Sci. Rep. 7 (2017) 12306, https://doi.org/10.1038/s41598-017-12502-4.
[45] F.A. Samad, T. Mohamed, Intensity and wavelength-dependent two-photon absorption and its saturation in ITO film, Appl. Phys. A 129 (2023) 31, https://doi.org/10.1007/s00339-022-06259-5.
[46] Á. Cubero, E. Martínez, L.A. Angurel, G.F. de la Fuente, R. Navarro, H. Legall, J. Krüger, J. Bonse, Surface superconductivity changes of niobium sheets by femtosecond laser-induced periodic nanostructures, Nanomaterials 10 (2020) 2525, https://doi.org/10.3390/nano10122525.
[47] A. Pan, A. Dias, M. Gomez-Aranzadi, S.M. Olaizola, A. Rodriguez, Formation of laser-induced periodic surface structures on niobium by femtosecond laser irradiation, J. Appl. Phys. 115 (2014) 173101, https://doi.org/10.1063/1.4873459.
[48] J.I. Goldstein, D.E. Newbury, P. Echlin, D.C. Joy, C. Fiori, E. Lifshin, X-ray spectral measurement: WDS and EDS. Scanning Electron Microscopy and X-Ray Microanalysis, Springer, Boston, MA, 1981, https://doi.org/10.1007/978-1-4613-3273-2_5.